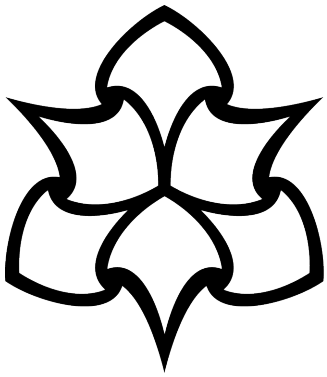

coatings

MDPI

Article

How do Graphene Composite Surfaces Affect the Development and Structure of Marine Cyanobacterial Biofilms?

Maria J. Romeu [1,2], Luciana C. Gomes [1,2], Francisca Sousa-Cardoso [1,2], João Morais [3], Vítor Vasconcelos [3,4], Kathryn A. Whitehead [5], Manuel F. R. Pereira [2,6], Olívia S. G. P. Soares [2,6] and Filipe J. Mergulhão [1,2,*]

1 LEPABE—Laboratory for Process Engineering, Environment, Biotechnology and Energy, Faculty of Engineering, University of Porto, Rua Dr. Roberto Frias, 4200-465 Porto, Portugal
2 ALiCE—Associate Laboratory in Chemical Engineering, Faculty of Engineering, University of Porto, Rua Dr. Roberto Frias, 4200-465 Porto, Portugal
3 CIIMAR—Interdisciplinary Centre of Marine and Environmental Research, University of Porto, Terminal de Cruzeiros do Porto de Leixões, Av. General Norton de Matos s/n, 4450-208 Matosinhos, Portugal
4 Department of Biology, Faculty of Sciences, University of Porto, Rua do Campo Alegre, 4169-007 Porto, Portugal
5 Microbiology at Interfaces, Manchester Metropolitan University, Chester Street, Manchester M1 5GD, UK
6 LSRE–LCM—Laboratory of Separation and Reaction Engineering–Laboratory of Catalysis and Materials, Faculty of Engineering, University of Porto, Rua Dr. Roberto Frias, 4200-465 Porto, Portugal
* Correspondence: filipem@fe.up.pt; Tel.: +351-225-081-668

Abstract: The progress of nanotechnology has prompted the development of novel marine antifouling coatings. In this study, the influence of a pristine graphene nanoplatelet (GNP)-modified surface in cyanobacterial biofilm formation was evaluated over a long-term assay using an in vitro platform which mimics the hydrodynamic conditions that prevail in real marine environments. Surface characterization by Optical Profilometry and Scanning Electron Microscopy has shown that the main difference between GNP incorporated into a commercially used epoxy resin (GNP composite) and both control surfaces (glass and epoxy resin) was related to roughness and topography, where the GNP composite had a roughness value about 1000 times higher than control surfaces. The results showed that, after 7 weeks, the GNP composite reduced the biofilm wet weight (by 44%), biofilm thickness (by 54%), biovolume (by 82%), and surface coverage (by 64%) of cyanobacterial biofilms compared to the epoxy resin. Likewise, the GNP-modified surface delayed cyanobacterial biofilm development, modulated biofilm structure to a less porous arrangement over time, and showed a higher antifouling effect at the biofilm maturation stage. Overall, this nanocomposite seems to have the potential to be used as a long-term antifouling material in marine applications. Moreover, this multifactorial study was crucial to understanding the interactions between surface properties and cyanobacterial biofilm development and architecture over time.

Keywords: antifouling surface; biofilm architecture; cyanobacterial biofilm; graphene; marine biofouling

Citation: Romeu, M.J.; Gomes, L.C.; Sousa-Cardoso, F.; Morais, J.; Vasconcelos, V.; Whitehead, K.A.; Pereira, M.F.R.; Soares, O.S.G.P.; Mergulhão, F.J. How do Graphene Composite Surfaces Affect the Development and Structure of Marine Cyanobacterial Biofilms? *Coatings* **2022**, *12*, 1775. https://doi.org/10.3390/coatings12111775

Academic Editor: Mohor Mihelčič

Received: 20 October 2022
Accepted: 17 November 2022
Published: 20 November 2022

1. Introduction

The oil, gas, and maritime industry are significantly impacted by biofouling, either through the costs related to the increased fuel consumption, hull cleaning, material deterioration, repainting, and corrosion [1], or even by the management intervention time and incorrect measurements in the submerged and moored sensors [2]. Ecologically, fouling events in marine environments promote species invasion and the establishment of exotic biofouling species in ports [3]. Moreover, biofouling can be a major concern in health-related problems since contamination of aquaculture facilities, such as fish cages, can occur by toxin accumulation, and air pollution may be increased through greenhouse gas emissions [4].

The non-toxic marine antifouling approaches available in the market are often expensive and not as effective as conventional biocides, which can accumulate in the marine environment and affect non-target aquatic organisms. Inorganic ingredient-based coatings have been used for biofouling prevention, including silver nanoparticles [5], carbon nanotubes (CNTs) [6], graphene [7], and metal oxides semiconductors such as zinc oxide (ZnO) [8] and titanium dioxide (TiO_2) [9]. Overall, antifouling marine paints containing nanomaterials have been reported to offer superhydrophobicity, microbial resistance, high durability, water repellency, anti-sticking, and anti-corrosive properties [10], being novel solutions for the sustainable development of the maritime industry. Advancements in materials technology have introduced carbon nanomaterials such as CNTs and graphene as a powerful approach for various applications in the marine and shipping industries [11]. Graphene consists of a single layer of carbon atoms arranged in a sp^2-bonded hexagonal pattern. It is considered one of the strongest and thinnest materials available, which shows high specific surface area, electrical conductivity, and thermal stability, making it appealing for different applications [12,13]. Moreover, due to its high strength level [14], this material is a breakthrough alternative in the naval industry. All these features make the application of graphene in technical processes of maritime industries attractive, such as in water management systems, desalination, removing toxic pollutants and filtering gasses, and as a coating material [15–17]. As a coating on marine structures, besides the anti-corrosive properties, graphene can also be used in de-icing surfaces for ship operations in extremely low-temperature regions, such as the Arctic and Antarctica, due to its electrical conductivity [15].

Nanotechnology-based technologies can be of great interest in creating novel low-toxic antifouling coatings [18]. However, analysis of the literature indicates that there is little information about the use of pristine graphene. Indeed, most in situ studies on graphene-based surfaces were performed with functionalized graphene and graphene oxide (GO) coatings [19–23]. Diatom adhesion was completely inhibited after 10 days by surfaces containing 0.36 wt% GO [24]. In turn, GO-silver nanoparticle coatings improved antibacterial and anti-algal properties [25], and showed more than 80% *Halomonas pacifica* biofilm inhibition [26]. Since the current trend is to study the potential of modified and functionalized graphene, the antibiofilm performance of graphene alone is poorly understood. Moreover, most in vitro studies are usually performed for short periods and under hydrodynamic conditions that do not mimic the real marine environment [27]. In fact, some of the in vitro studies have been performed until 24 h [6,23,25,28,29], most of them between days and weeks [7,19,20,24,30–33], but only a study performed by Fazli-Shokouhi et al. [34] extended the assay period for 3 months to evaluate the antifouling potential of graphene-based coatings. Moreover, these studies focus on organisms other than cyanobacteria, namely diatoms, algae, and macrofoulers. Therefore, the main goal of this work was to evaluate the potential of a graphene composite surface to prevent and control the development of biofilms by marine microfoulers over a long-term assay and using an in vitro platform that mimics the hydrodynamic conditions found in real marine scenarios. Cyanobacterial biofilm architecture was evaluated by three different imaging techniques: Optical Coherence Tomography (OCT), Confocal Laser Scanning Microscopy (CLSM), and Scanning Electron Microscopy (SEM). Since the epoxy resin is a commercially available coating generally used to coat the hulls of small recreational vessels [35,36] due to its exceptional physical, chemical, and mechanical properties, no safety issues, and low cost [37], pristine graphene nanoplatelets (GNP) were incorporated into this polymer matrix. Furthermore, epoxy composites exhibited high durability and resistance to fatigue and UV irradiation [38]. Surface characterization was also performed by water contact angle measurements, Optical Profilometry, and SEM.

2. Materials and Methods

Figure 1 presents the flowchart of the experimental work fully described in the upcoming sections.

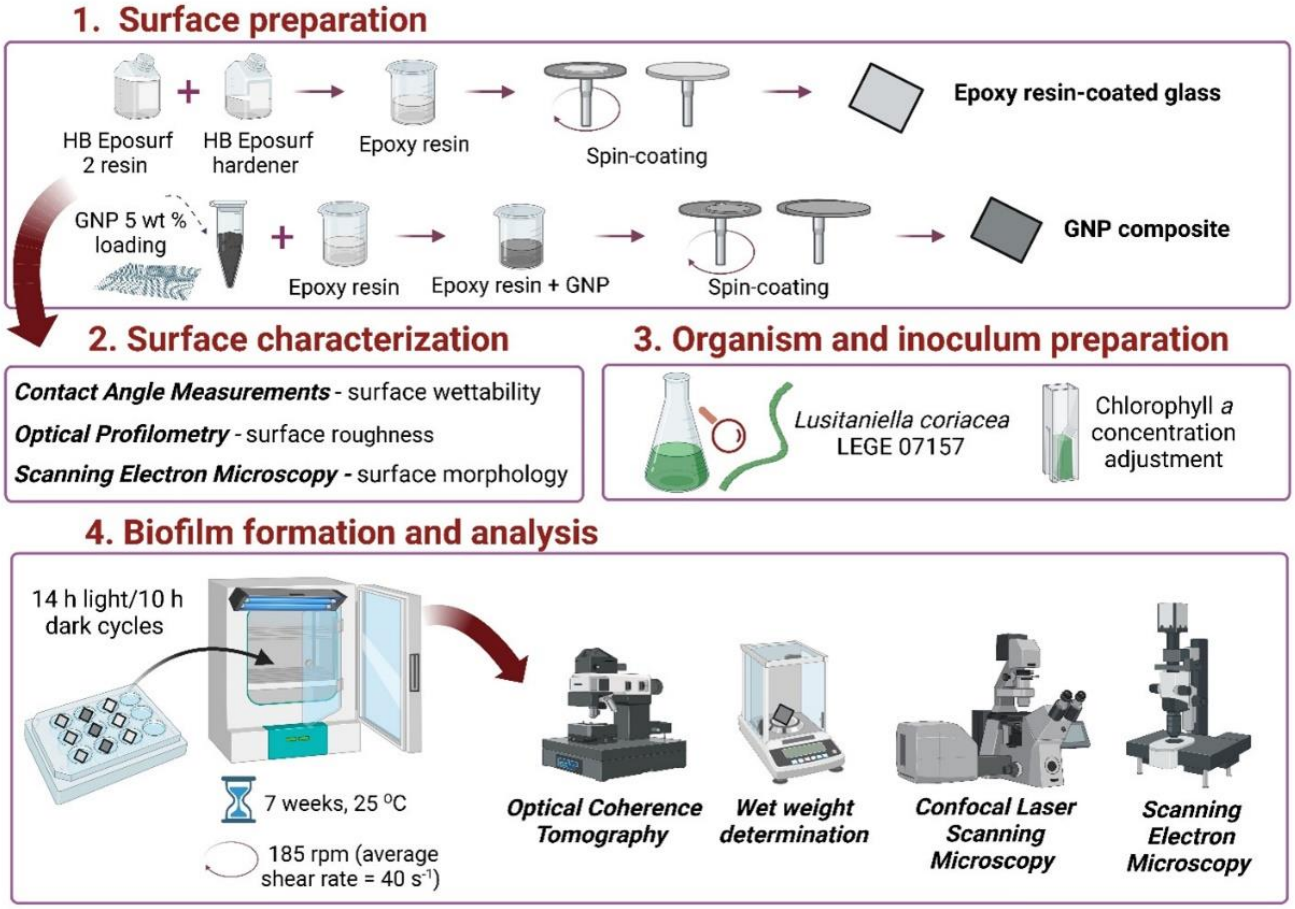

Figure 1. Scheme of the experimental steps of the present work.

2.1. Surface Preparation

Two control surfaces (glass, a commonly submerged artificial surface found on diverse equipment in aquatic environments, and epoxy resin, a commercially available marine coating) and a GNP composite were tested to determine their performance against cyanobacterial biofilm development. The epoxy resin-coated glass was prepared following the protocol described by Faria et al. [39]. Briefly, HB Eposurf 2 resin and HB Eposurf hardener, both from HB Química (Matosinhos, Portugal), were mixed in a ratio of 10:3 (*v*/*v*). To produce the epoxy resin-coated surfaces, 70 µL of the above mixture was placed on top of 1 cm × 1 cm glass coupons (Vidraria Lousada, Lda, Lousada, Portugal) using a spin coater (Spin150 PolosTM, Paralab, Porto, Portugal) at 6000 rpm for 40 s. After 12 h at room temperature, the surfaces were dried for 3 h at 60 °C.

The methodology for the preparation of the GNP composite was adapted from Oliveira et al. [40], in which the polydimethylsiloxane (PDMS) matrix was replaced by the epoxy resin. Briefly, after mixing the two epoxy resin components, 5 wt% of GNPs aggregates (Alfa Aesar, Thermo Fisher Scientific, Erlenbachweg, Germany) were incorporated into the epoxy resin mixture. The specific surface area (S_{BET}), external surface area (S_{meso}), micropore volume (V_{micro}), and total pore volume (V_p) of these GNPs are 464 $m^2\ g^{-1}$, 363 $m^2\ g^{-1}$, 0.045 $cm^3\ g^{-1}$, and 0.535 $cm^3\ g^{-1}$, respectively [40]. In the same study [40], 5 wt% was demonstrated to be an effective load in reducing single- and mixed-species biofilms of *Pseudomonas aeruginosa* and *Staphylococcus aureus* formation after 24 h. After the incorporation step, 70 µL of the composite (5 wt% GNP/epoxy resin) was deposited on glass squares by spin coating.

2.2. Surface Characterization

2.2.1. Wettability

The measurement of water contact angles (θ_w) was performed through the sessile drop method using an SL200C optical contact angle meter (Solon Information Technology Co., Ltd., Shanghai, China) as previously described [41,42]. At least 25 determinations for each material at room temperature were performed.

2.2.2. Optical Profilometry

Optical profilometry was used to determine the average roughness (S_a) of the glass, epoxy resin, and GNP composite surfaces, as previously performed by Whitehead et al. [43,44]. A MicroXAM surface mapping microscope (ADE Corporation, XYZ model 4400 mL system, Tucson, AZ, USA), with an objective of 50× and connected to an AD phase shift controller (Omniscan, Wrexham, UK), was used to image five areas (167 µm × 167 µm) of at least four different coupons. The MapView AE 2.17 software (Omniscan, Wrexham, UK) was chosen to determine the (S_a) values through extended range vertical scanning interferometry, and the 3D images were extracted by SPIP™ 6.7.9 software (Image Metrology A/S, Hørsholm, Denmark).

2.2.3. Scanning Electron Microscopy (SEM)

The surface morphology of the three surfaces used in this study was investigated using SEM. The surfaces were placed on SEM stubs (Agar Scientific, Stansted, UK) and sputter-coated with gold for 30 s in an SEM coating system (Polaron, London, UK). The secondary electron detector of a Supra 40VP scanning electron microscope (Carl Zeiss Ltd., Cambridge, UK) was used to obtain images of at least three coupons for each surface at an accelerating voltage of 2 kV.

2.3. Organism and Inoculum Preparation

A filamentous cyanobacterial strain *Lusitaniella coriacea* LEGE 07157 was obtained from the Interdisciplinary Centre of Marine and Environmental Research (CIIMAR), Matosinhos, Portugal [45]. *Lusitaniella coriacea* LEGE 07157 was isolated by rock surface scraping from a zone tide pool at Lavadores beach, Porto, Portugal (41.12919 N 8.668578 W). It was grown in Z8 medium [46] enhanced with 25 g L^{-1} of synthetic sea salts (Tropic Marin) and vitamin B_{12} (Sigma Aldrich, Merck, Saint Louis, MO, USA), and at 25 °C under 14 h light (10–30 µmol photons m^{-2} s^{-1}, λ = 380–700 nm)/10 h dark cycles, as recommended by Ramos et al. [45].

2.4. Biofilm Formation

Cyanobacterial suspensions were adjusted to a chlorophyll *a* concentration of 1.22 ± 0.09 µg mL^{-1} since this pigment is unique and predominant in all groups of cyanobacteria and its quantification is a standard methodology to estimate the biomass in marine environments [47,48]. Briefly, cyanobacterial cells were collected by centrifugation (3202× *g* for 5 min) and a volume of 2 mL of 99.8% methanol (Methanol ACS Basic, Scharlau Basic, Barcelona, Spain) was added. After 24 h of dark incubation at 4 °C, cyanobacterial suspensions were centrifuged and absorbance measurements of the supernatant were performed at 750 nm (turbidity), 665 nm (chlorophyll *a*), and 652 nm (chlorophyll *b*) (V-1200 spectrophotometer, VWR International China Co., Ltd., Shanghai, China). The values obtained were used to calculate chlorophyll *a* concentration (µg·mL^{-1}) through Equation (1) [49]:

$$Chl\ a\ \left(\mu g \cdot mL^{-1}\right) = 16.29 \times A^{665} - 8.54 \times A^{652} \quad (1)$$

Biofilm formation was tested on agitated 12-well plates (VWR International, Carnaxide, Portugal) under previously optimized conditions for cyanobacterial biofilm development [47]. All coupons and plates were subjected to UV sterilization, after which

the coupons were fixed on double-sided adhesive tape [40,47]. A volume of 3 mL of the adjusted cyanobacterial suspension was added to each well. To mimic the hydrodynamic conditions found in marine environments, microplates were then incubated at 25 °C in a shaker with a 25 mm orbital diameter (Agitorb 200ICP, Norconcessus, Ermesinde, Portugal) at 185 rpm, resulting in an average shear rate of 40 s^{-1} [47]. Biofilm formation in this platform includes the shear rate valued for a ship in a harbor, 50 s^{-1} [50], and it was shown to predict the biofouling behavior observed upon immersion in the sea for prolonged periods [51]. Moreover, to simulate marine biofilm formation on submerged surfaces, microtiter plates were kept under 14 h light (8–10 µmol photons m^{-2} s^{-1})/10 h dark cycles [47,52,53]. The light intensity was decreased from 10–30 µmol photons m^{-2} s^{-1} to 8–10 µmol photons m^{-2} s^{-1} because biofouling organisms have reduced access to light when in immersion (either by the effect of the marine equipment/device/ship to which they are attached, or by the influence of the biofilm structure in which the accumulation of different organisms occurs, and some of them are located in the inners layers of biofilm). Since a 2-month interval for maintenance is the minimum time for economically viable underwater monitoring systems [47], biofilm development was followed for 7 weeks (49 days), and during this incubation time, the medium was changed twice a week in the sample and control wells.

2.5. Biofilm Analysis

Two coupons of each surface were analyzed every 7 days. For that, the culture medium was removed and the wells were filled with 3 mL of sodium chloride solution (8.5 g L^{-1}) [47]. The solution was carefully removed and the wells were filled again with 3 mL of sodium chloride to assess the cyanobacterial biofilm structure through Optical Coherence Tomography (OCT). The determination of biofilm wet weight was also performed over 7 weeks, and at the end of the experiment (49 days), cyanobacterial biofilm architecture and morphology were analyzed by Confocal Laser Scanning Microscopy (CLSM) and SEM, respectively.

2.5.1. Optical Coherence Tomography (OCT)

Images from cyanobacterial biofilms were captured as reported by Romeu et al. [47] through OCT (Thorlabs Ganymede Spectral Domain Optical Coherence Tomography system with a central wavelength of 930 nm, Thorlabs GmbH, Dachau, Germany). Briefly, for each coupon, 2D imaging was performed (with a minimum of 2 fields of view) and evaluated through a routine developed in the Image Processing Toolbox from MATLAB 8.0 and Statistics Toolbox 8.1 (The MathWorks, Inc., Natick, MA, USA) [54]. The mean of biofilm thickness was calculated according to Equation (2):

$$\overline{L}_F = \frac{1}{N}\sum_{i=1}^{N} L_{F,i} \quad (2)$$

where $L_{F,i}$ is a local biofilm thickness measurement at location i, N equals the number of thickness measurements, and $\overline{L}_F$ is the mean biofilm thickness. The percentage of empty spaces in the biofilm structure, as well as their average size, was also assessed [55].

2.5.2. Wet Weight Determination

The determination of the biofilm wet weight was performed as previously reported [56] and considered as the difference from the initial coupon weight determined before inoculation.

2.5.3. Confocal Laser Scanning Microscopy (CLSM)

Biofilms with 49 days were stained with 6 µM SYTO®61 (Thermo Fisher Scientific, Waltham, MA, USA), mounted on a microscopic slide, and observed in a Leica TCS SP5 II Confocal Laser Scanning Microscope (Leica Microsystems, Wetzlar, Germany) with a 40× water objective lens (Leica HCX PL APO CS 40.0x/1.10WATER UV) and 633-nm helium-neon laser. Image stacking was acquired with a z-step of 1 µm for each sample at a

minimum of five random fields of 387.5 μm × 387.5 μm (equivalent to 512 pixels × 512 pixels. The "Easy 3D" tool of the IMARIS 9.1 software (Bitplane, Zurich, Switzerland) was used to create 3D projections of the biofilms. Additionally, biofilm architectural parameters such as biovolume (μm^3 μm^{-2}) and surface coverage (%) were determined using the COMSTAT image-analysis software [57].

2.5.4. SEM

After 49 days of incubation, *Lusitaniella coriacea* LEGE 07157 biofilms grown on the three tested surfaces were observed by SEM. Samples were taken from the microplates, dehydrated with increasing ethanol concentrations (10, 25, 40, 50, 70, 80, 90, and 100% (*v*/*v*)), and left in a desiccator until microscopic analysis [58]. Then, they were sputter-coated using the equipment and conditions described before and imaged in the Supra 40VP scanning electron microscope.

2.6. Statistical Analysis

Two biological experiments with two technical replicates each were analyzed. Quantitative parameters obtained from biofilm wet weight, OCT, and CLSM were compared using one-way ANOVA with Tukey's multiple comparisons test (GraphPad Prism® version 6.01, GraphPad Software, Inc., San Diego, CA, USA). Statistically significant differences between the different surfaces for the same sampling day were considered for p values < 0.05 (corresponding to a confidence level greater than 95%). The error bars represent the standard deviation (SD) of the mean.

3. Results and Discussion

3.1. Surface Analysis

It is known that surface properties, including wettability, roughness, and morphology, are important factors governing initial bacterial adhesion to surfaces and consequently affect the development of mature biofilms [59]. Therefore, the three tested surfaces (glass, epoxy resin, and GNP composite) were evaluated regarding (i) wettability by water contact angle measurements, (ii) topography and roughness by Optical Profilometry, and (iii) morphology by SEM.

Results obtained from water contact angle measurements are shown in Figure 2a. Contact angle determination provides information about the wettability of the surface, i.e., the tendency of the fluid to spread on a surface, and the hydrophobicity of the surface, which describes the tendency of non-polar molecular aggregation and, consequently, water molecule repulsion [60]. Surfaces can be classified as superhydrophilic, hydrophilic, hydrophobic, or superhydrophobic, if the contact angle of water with the surfaces is lower than 10°, between 10° and 90°, between 90° and 150°, or over 150°, respectively [61]. While glass is considered hydrophilic (θ_w = 40.9° ± 7.4°), the GNP composite (θ_w = 68.6° ± 2.4°) and epoxy-coated surfaces (θ_w = 76.3° ± 2.5°) are slightly more hydrophobic than glass. The wettability of the epoxy resin was weakly affected by the incorporation of graphene on the coating; the GNP composite is slightly more hydrophilic than the resin. Similar results were observed in previous studies [40,62]. In fact, in a study performed by Rafiee et al. [62], the water contact angle of a copper substrate coated with graphene was up to 90.6°, while that of the pure copper substrate was about 85.9°. Oliveira and her coworkers [40] also verified that 5 wt% GNP/PDMS and PDMS surfaces presented similar water contact angles, 121.8° and 110.2°, respectively. Since the wetting properties at the water–graphene interface had little effect on the water–substrate interaction, this peculiar wettability of graphene has been described by the term "wetting transparency of graphene" [62]. In the present study, as dispersed GNPs were used instead of graphene layers, it is conceivable to assume that the wettability of the substrate may be even less affected by the presence of graphene.

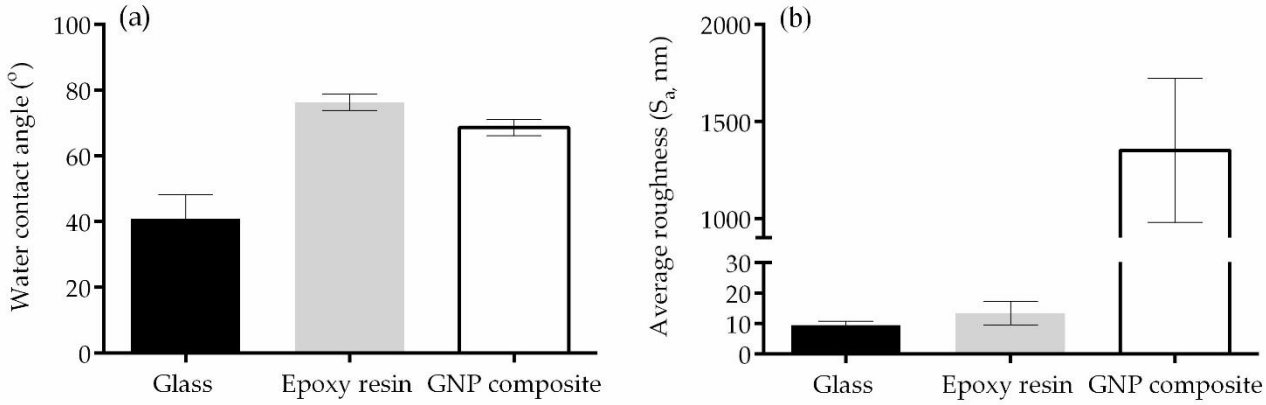

Figure 2. Water contact angles (**a**) and average roughness (S_a) (**b**) of the tested surfaces. The means ± SD are shown.

Results obtained from roughness analysis are shown in Figures 2b and 3. The GNP composite was the roughest surface (S_a = 1351 nm), followed by the epoxy resin (S_a = 13 nm) and glass (S_a = 10 nm). Therefore, the average roughness values of both control surfaces are on the nanometric scale, being about 1000 times lower than the roughness value determined for the GNP composite (Figure 2b). The difference in roughness and topography between the graphene composite and both control surfaces (glass and epoxy resin) is particularly evident in the 3D images of the surfaces given by profilometry (Figure 3). While glass and resin without incorporated carbon material were homogeneous and smooth surfaces (Figure 3a,b, respectively), the nanocomposite presented some irregularities distributed along the analyzed surface area (Figure 3c). Looking at the SEM images (Figure 4c,d), it was possible to confirm that these surface elevations correspond to agglomerated graphene nanoplatelets in the polymer matrix. Some of the larger agglomerates had sizes ranging from 7–30 µm.

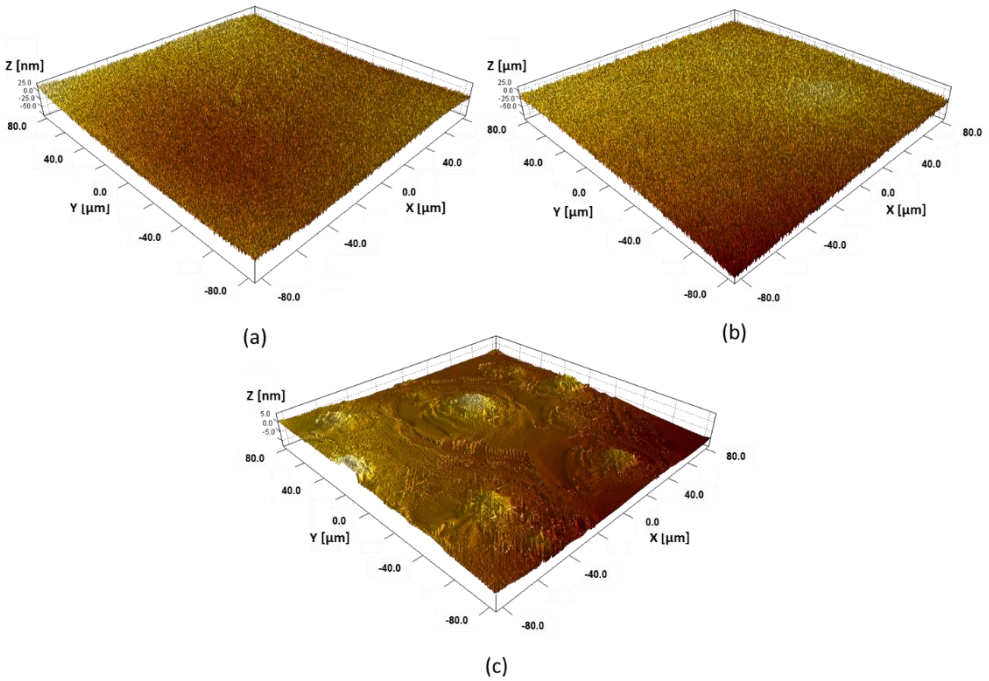

Figure 3. 3D profilometer images of glass (**a**), epoxy resin (**b**), and GNP composite (**c**).

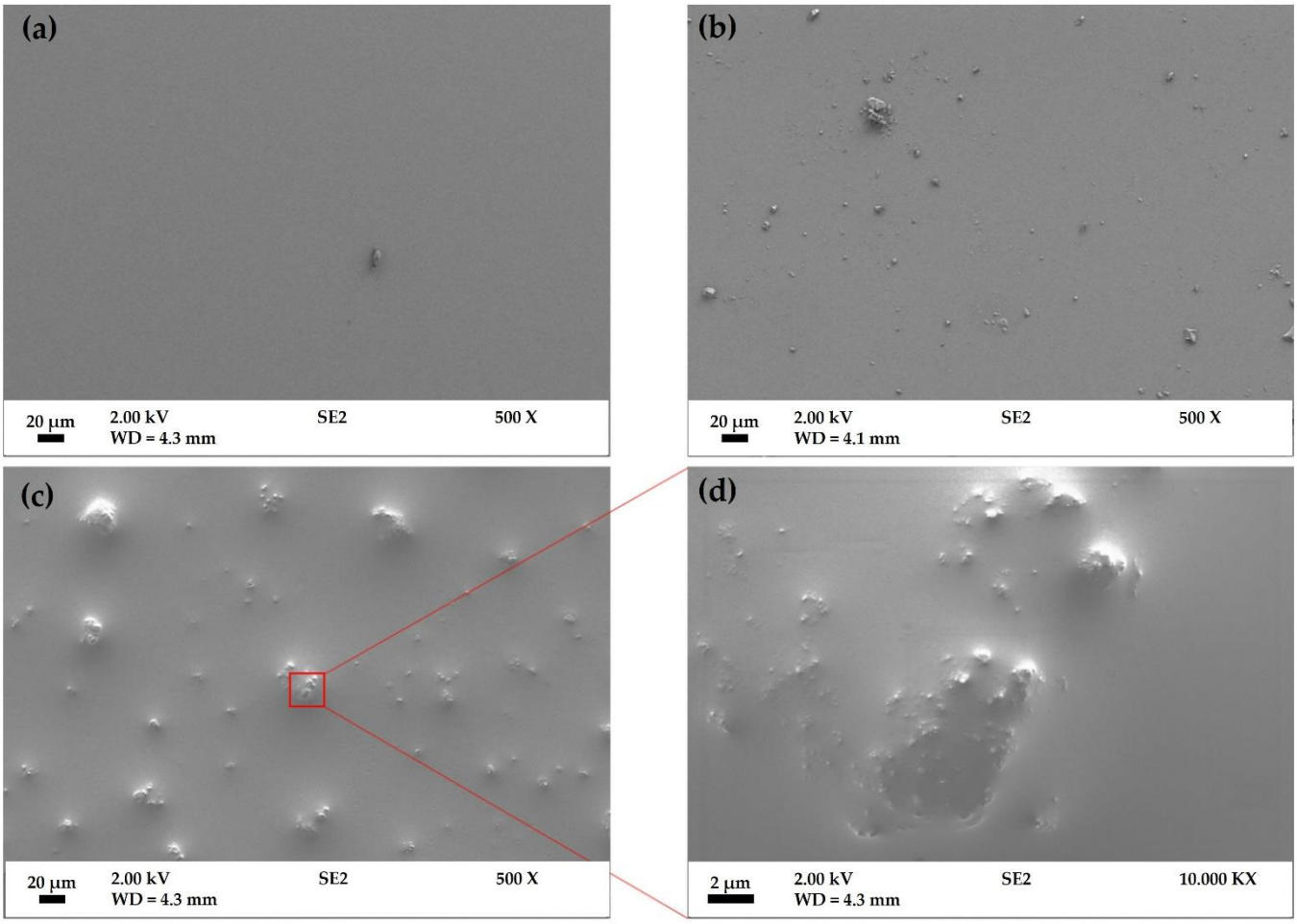

Figure 4. SEM images of glass (**a**), epoxy resin (**b**), GNP composite (**c**), and magnified GNP composite (**d**). The micrographs have a magnification of 500×, except for (**d**), which corresponds to a higher magnification image (10,000×) of the surface area marked in red in (**c**).

It is a challenge to disperse GNPs, especially compared to other carbon materials such as CNTs, due to the van der Waals forces and a strong π–π interaction between the individual GNP sheets, which are responsible for their layer-stacked compact structure [40,63]. Their incorporation in the polymeric resin may facilitate graphene dispersion, thus reducing the tendency to aggregate [64]. In the higher magnification image of the GNP composite (Figure 4d), it was interesting to detect some areas on top of the embedded GNP clusters where this carbon material was more exposed. It is described that one of the factors directing the antimicrobial activity of graphene is the agglomeration tendency, which causes a reduced surface area and shape alteration [65,66]. However, the presence of more exposed GNPs in the epoxy resin may facilitate their interaction with the microorganisms that come in contact with the surface, triggering the predominant antimicrobial mechanisms of this carbon nanomaterial—oxidative stress, mechanical damage of cell membrane/wall by nanoknives, and wrapping/trapping [66,67].

In vitro assays showed that no detectable leaching occured under the conditions used in this work as assessed by UV-Vis spectroscopy (data not shown).

3.2. Biofilm Development

As there are several mechanisms affecting the microbial response and the disruption of biofilm architecture, the long-term antifouling properties of a given surface for marine applications should be extensively studied. Although the Minimal Inhibitory Concentration (MIC) of the studied GNPs could not be determined for *Lusitaniella coriacea* LEGE 07167 (it is

a filamentous cyanobacterium and therefore cell numbers cannot be accurately determined), it was found to be higher than 5% (*w*/*v*, in a VNSS suspension assay) for a model marine bacterium (*Cobetia marina*). Cyanobacterial biofilm development was monitored over 7 weeks (49 days) and the quantitative results obtained from wet weight determination and 2D OCT analysis are shown in Figure 5. The values regarding the biofilm thickness, the percentage of empty spaces, and the average size of empty spaces on biofilm structure (Figure 5b–d) are indicated from day 14 since the biofilm thickness was below the OCT range on the first sampling day. Although a progressive increase in biofilm development was observed from the results of wet weight (Figure 5a) and biofilm thickness (Figure 5b), this evolution over the 7 weeks was more noticeable on glass and epoxy resin than on the GNP composite. Indeed, for biofilm wet weight (Figure 5a), from day 7 to day 49, an increase of 84 %, 77 %, and 67 % was observed for glass, epoxy resin, and GNP composite, respectively, while for biofilm thickness (Figure 5b), from day 14 to day 49, an increase of 85 %, 86 %, and 58 % was observed for the same surfaces. This behavior was also seen regarding biofilm architecture (Figure 5c) given that an increase of 92 %, 98 %, and just 28 % for the percentage of empty spaces was observed on glass, epoxy resin, and GNP composite. This suggests that graphene-modified surfaces may delay biofilm development (Figure 5a,b) and change its structure to a less porous arrangement (Figure 5c). Additionally, on days 35, 42, and 49, a reduction of biofilm wet weight and thickness was observed on the GNP composite surface when compared to the epoxy resin itself. In fact, on days 35, 42 and 49, the wet weight values obtained for the GNP composite were 46 %, 47 %, and 44 % lower than those obtained on the epoxy resin surface, respectively (Figure 5a). For biofilm thickness on the same days, the values obtained on the GNP composite were 46 %, 42 %, and 54 % lower than those obtained on the epoxy resin surface, respectively (Figure 5b). The delay effect caused by this carbon nanomaterial on cyanobacterial biofilm development, as well as the greater antifouling effect on the maturation stage of biofilm development, was also observed in previous work where CNT-modified surfaces were used as potential antifouling surfaces [42]. In addition, in the maturation stage of biofilm development (days 42 and 49), a lower percentage of empty spaces (Figure 5c) and an average size of empty spaces on biofilm structure (Figure 5d) were detected for biofilms formed on the GNP composite when compared with control surfaces (glass and epoxy resin).

Figure 6 shows representative 2D cross-sectional images of *Lusitaniella coriacea* LEGE 07157 biofilm development on glass, epoxy resin, and GNP composite after 49 days. These images corroborate the quantitative data obtained from biofilm biomass (Figure 5a,b) and empty spaces on biofilm architecture (Figure 5c,d) since a lower amount of biofilm mass and percentage of empty spaces and its average size were observed on the GNP composite compared to the control epoxy resin. Although the reduced biofilm development on the GNP-based coating may be beneficial for the performance of marine devices and/or equipment, the efficacy of chemical methods to eradicate biofilms formed on this surface material may be hampered. Given the lower percentage of empty spaces and their smaller average size shown in biofilms formed on the GNP composite, the diffusion of chemical compounds typically used for biofouling control through the inner layers of the biofilm may be hindered [68]. The biofilm structure could also be compared between the three surfaces. While a flatter and homogeneous biofilm was observed on glass (Figure 6a), biofilms formed on the epoxy resin (Figure 6b) and GNP composite (Figure 6c) had heterogeneous shapes. Additionally, more streamers could be observed on top of the biofilm developed on the epoxy resin surface (Figure 6b), which probably contributed to the higher thickness of biofilms developed on this surface compared to the GNP composite (Figure 5b). Opposing results were obtained in a previous study focused on CNT-based surfaces [42], in which a flatter and homogeneous cyanobacterial biofilm was observed on the CNT composite. However, this divergent finding may be related to the use of a different cyanobacterial strain and carbon-based surface.

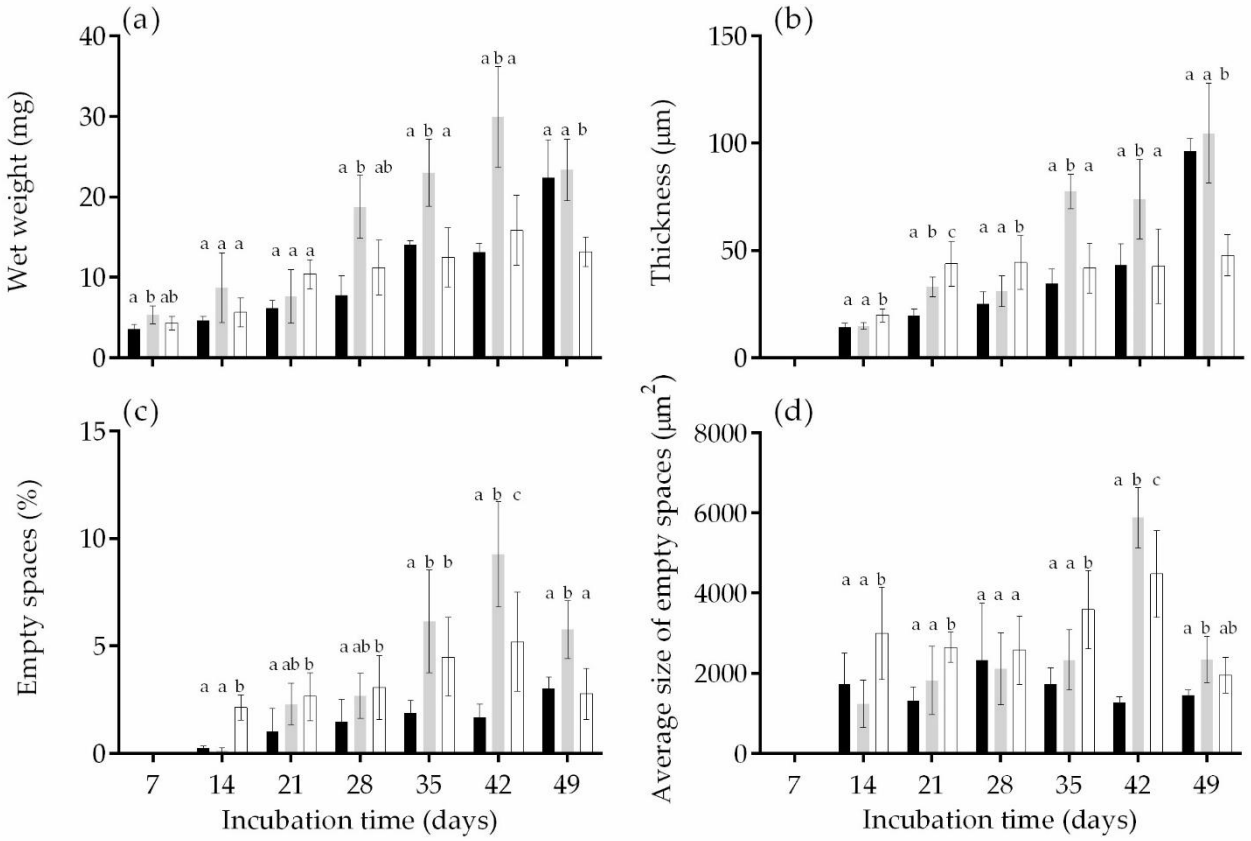

Figure 5. *Lusitaniella coriacea* LEGE 07157 biofilm development on different surfaces: glass (black), epoxy resin (grey), GNP composite (white). The parameters analyzed refer to biofilm wet weight (**a**), biofilm thickness (**b**), average percentage of empty spaces (**c**), and their respective average size (**d**) on biofilm structure. Mean values and SD from two biological assays with two technical replicates each are represented. For each sampling day, different lowercase letters (a, b, and c) indicate significant differences between surfaces ($p < 0.05$).

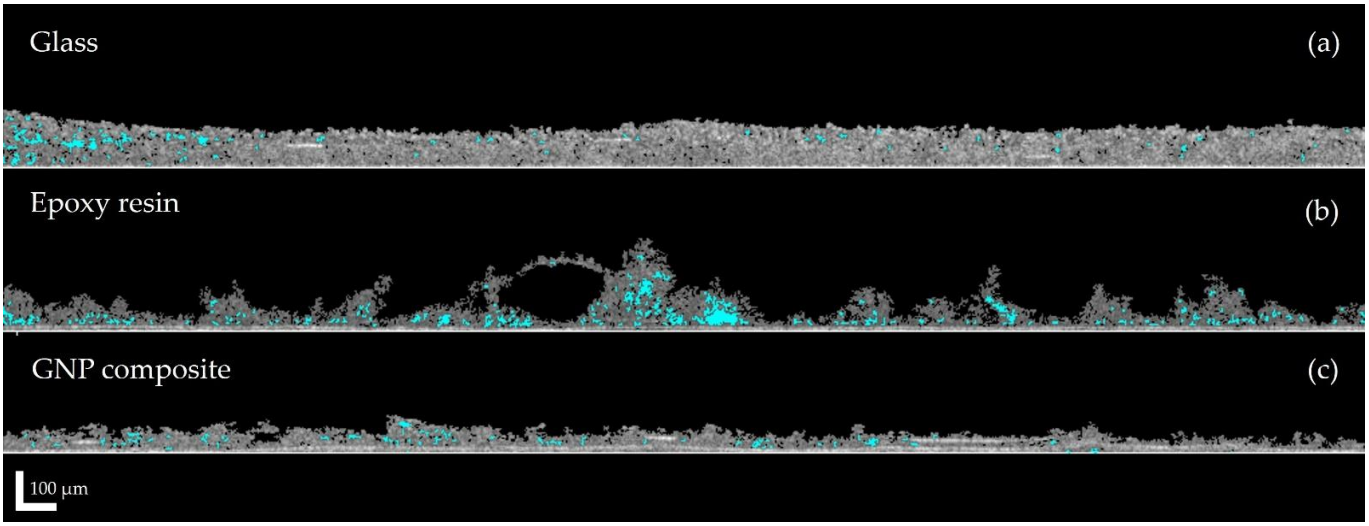

Figure 6. Representative 2D cross-sectional OCT images obtained for *Lusitaniella coriacea* LEGE 07157 biofilms on glass (**a**), epoxy resin (**b**), and GNP composite (**c**) after 49 days. The empty spaces on the biofilm structure are indicated in blue (scale bar = 100 µm).

Comparing the biofilm structure over the 49 days (Figure 5b,c), it was possible to observe different patterns between biofilms formed on the epoxy resin without and with

embedded GNPs. In the early stages of biofilm formation (days 14 to 28), biofilms formed on the GNP composite were thicker and presented a higher percentage of empty spaces when compared to the epoxy resin surface, while in the maturation phase (days 35 to 49) these parameters became lower. These findings suggest that the higher roughness of the GNP composite may initially promote the development of a porous and thicker biofilm, and at the maturation stage, a biofilm structural arrangement may occur. In fact, 2D cross-sectional OCT images obtained for *Lusitaniella coriacea* LEGE 07157 biofilms after 28 days (Figure S1 in Supplementary Material) revealed that biofilms formed on the GNP composite presented a higher number of streamers than the older biofilm (Figure 6c). Initially, to avoid the direct contact with GNP present on epoxy resin, cyanobacterial cells may have adapted their adhesion for vertical biofilm growth rather than a homogeneous development along the surface, contributing to the higher values of thickness between days 14 and 28. Although some previous studies revealed that the first dead cells could prevent the direct contact of live cells with graphene oxide (GO) surfaces, serving as a nutrient for live cells and consequently enhancing biofilm formation [69], the differences in architectural adaptation observed over time may provide an additional explanation for the antibiofilm mechanisms of the GNP composite. Indeed, values obtained from the biofilm roughness coefficient (Figure S2 in Supplementary Material) showed that all biofilms formed on day 28 presented a higher roughness compared with biofilms developed on day 49 ($p < 0.05$), including biofilms formed on the GNP composite.

Moreover, it was also hypothesized that the inability of *Lusitaniella coriacea* LEGE 07157 to form a dense and robust biofilm on the GNP composite was related to the damaging effect of graphene in the first cells adhered to the surface. These bacterial cells could be affected by the higher roughness of the graphene-based nanocomposite since the surface peaks corresponding to GNP clusters may directly affect bacterial viability by increasing the surface contact area and, consequently, the piercing action of exposed graphene particles. These initial adhered cells would become more fragile, probably leading to the improper adherence of the following layers of cells and hindering long-term biofilm formation. In previous work, Oliveira et al. [70] showed that 5 wt% GNP/PDMS surfaces reduced the number of total (57%), viable (69%), culturable (55%), and VBNC cells (85%) of 24-h *S. aureus* biofilms compared to PDMS [40]. Besides cell death, the increased permeability of cell membranes caused by nanoparticles may affect extracellular polymeric substances (EPS) production, resulting in a disrupted 3D structure of biofilm.

The CLSM analysis was performed to analyze structural differences between the biofilms formed on the three tested surface materials (glass, epoxy resin, and GNP composite; Figure 7). While the 49-day-old biofilm developed on glass was dense, preventing the observation of individual filaments on the cyanobacterial cells in the top view (Figure 7a), the biofilms formed on epoxy resin surfaces without and with GNPs (Figure 7b,c, respectively) displayed randomly distributed filaments. Furthermore, a drastic reduction in total biofilm amount was observed on the GNP composite when compared to both glass and epoxy resin surfaces. This was corroborated by the quantitative data extracted from the confocal stacks (Figure 7d,e), in which a decrease in biovolume (on average 86%, $p < 0.05$; Figure 7d) and surface coverage (on average 65%, $p < 0.05$; Figure 7e) was observed on the graphene-based surface compared to control surfaces.

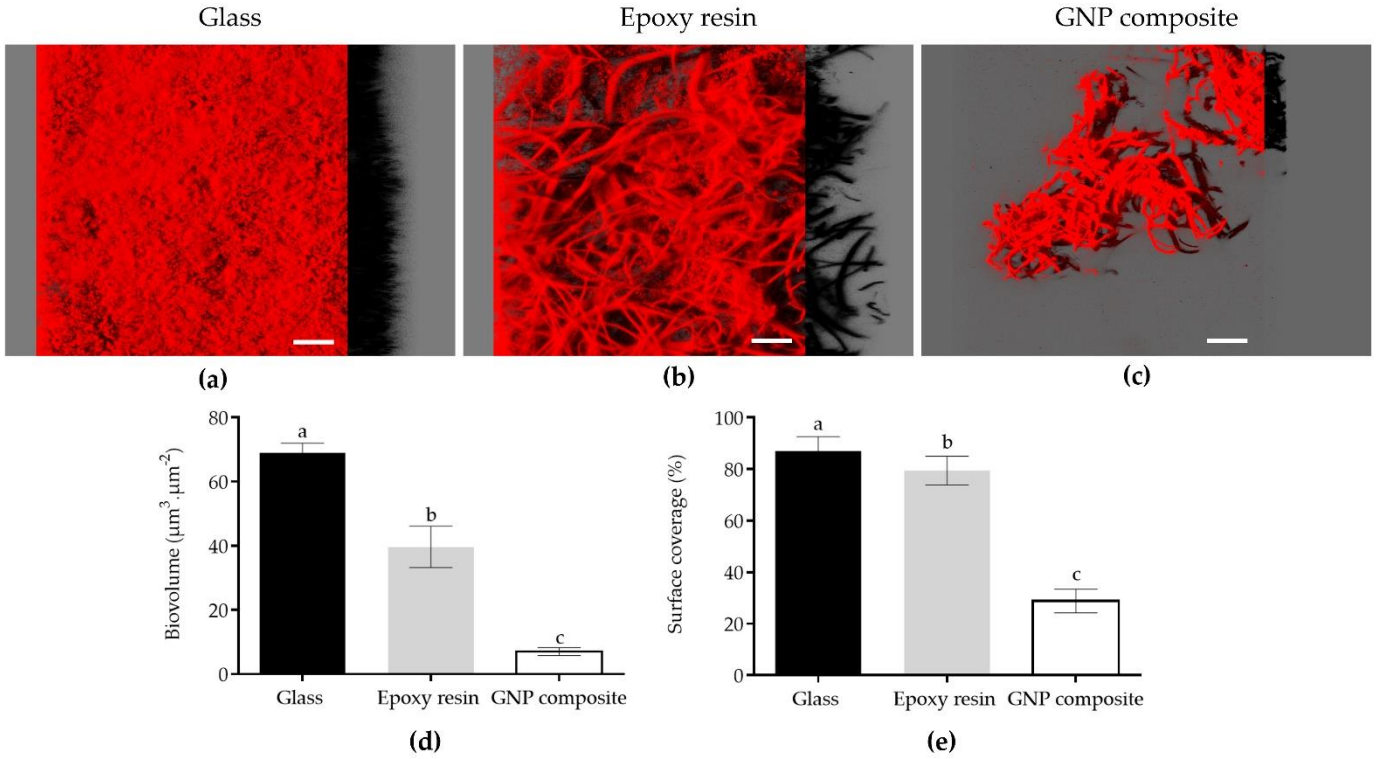

Figure 7. Three-dimensional confocal reconstructions of *Lusitaniella coriacea* LEGE 07157 biofilms grown on (**a**) glass, (**b**) epoxy resin, and (**c**) GNP composite after 49 days of incubation (white scale bars = 50 µm). These images show the biofilm aerial view, with the virtual shadow projection on the right (representative of biofilm thickness). Biovolume (**d**) and surface coverage (**e**) values of cyanobacterial biofilms were extracted from confocal files with the COMSTAT program. The means ± SD are presented. Different letters in the graphs (a, b, and c) indicate a significant difference among surfaces ($p < 0.05$).

The morphology of 49-day-old *Lusitaniella coriacea* LEGE 07157 biofilms on glass, epoxy resin, and GNP composite surfaces was also studied by SEM (Figure 8). The appearance of the biofilm developed on each surface was different, particularly when comparing the biofilm formed on glass (Figure 8a) with that formed on the epoxy resin without and with GNPs (Figure 8b,c, respectively). Indeed, the biofilm formed on the glass surface was very dense, and filamentous cyanobacteria were completely embedded in a complex matrix, which is a crucial feature of biofilm formation, making it impossible to distinguish the morphology of the individual *Lusitaniella coriacea* cells. Contrariwise, the electron micrograph of the epoxy resin surface (Figure 8b) displayed mesh-like structures around the *Lusitaniella* cells (possibly resulting from exopolysaccharide secretion), and filaments made of chains of cells that covered the entire surface and which were arranged in random directions. The cyanobacterial filaments were even more visible in the biofilm formed on the GNP composite, where the amount of extracellular material seemed to be lower and where uncovered areas of surface areas could be seen (Figure 8c). Therefore, SEM observations corroborated the results of the biofilm wet weight (Figure 5a), and those obtained by OCT (Figure 6) and CLSM (Figure 7), indicating that the graphene composite surface had a lower biofilm amount than the control surfaces after 49 days. Likewise, SEM micrographs also supported the finding that GNP-modified surfaces may decrease EPS production, resulting in a disrupted 3D structure of biofilm at the maturation stage. Similar results were obtained on CNT-based surfaces compared to the control surfaces (glass and epoxy resin) since SEM images of cyanobacterial biofilm grown on the CNT composite presented lower-density cell aggregates [42].

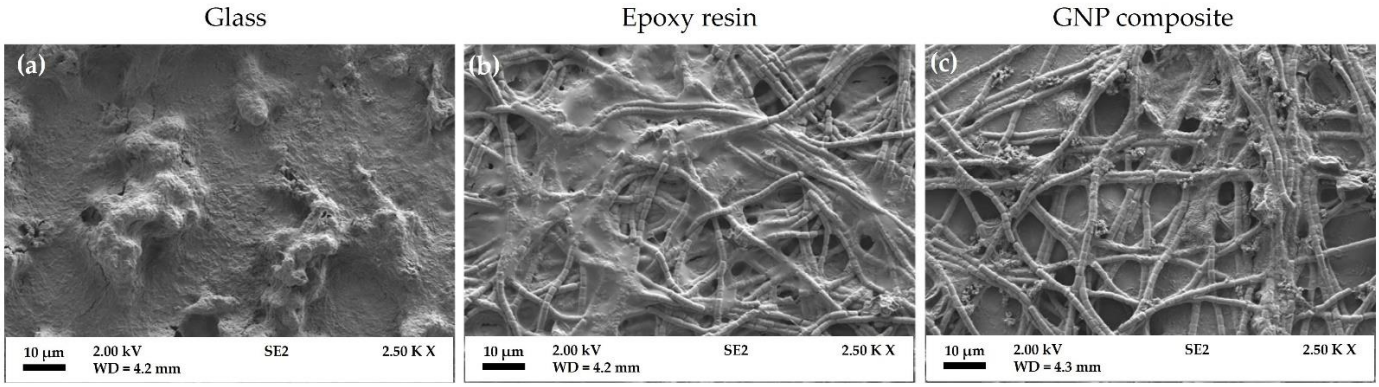

Figure 8. SEM micrographs of *Lusitaniella coriacea* LEGE 07157 biofilms grown on glass (**a**), epoxy resin (**b**), and GNP composite (**c**) after 49 days of incubation. Magnification = 2500×; scale bar = 10 µm.

This work may be limited by the use of cyanobacterial monocultures, the lack of field tests, and the absence of surface tribological characterization for long periods of immersion. Taking into account that the most studied forms of graphene within the marine context are GO and GO functionalized with metal nanoparticles [27], further experimental assays with other graphene-based surfaces for the marine environment should be performed. These assays can comprise different physical and chemical properties (e.g., dimension, number of layers, and functionalization), but also focus on factors related to the production of the surface (e.g., graphene loading, nanoparticle dispersion, and aggregation) [71–73]. Future in situ studies should also include other foulers, as well as being performed for a longer period since, in the present study, a distinct effect was observed over time. In fact, few studies on graphene-based surfaces were performed over one [19,20] or more months [34]. Although different optical techniques have been used in this study, further work should assess the metabolic state and the viability of biofilm cyanobacterial cells [74,75]. Omics approaches such as transcriptomic analysis to consider the expression of virulence factors and adhesion genes related to biofilm development [30], and proteomic analysis to elucidate cyanobacterial defense mechanisms to graphene toxicity, should also be considered [52,54,56]. Moreover, computational simulation approaches have been widely used for the characterization of novel materials [76]. Strong coupling between experimental data and numerical simulation is required for predicting macroscopic behavior with a fine description of local fields. By combining modeling approaches and corresponding experiments, the studies take advantage of the simplicity, efficiency, and mechanistic insight gained from the models, and the physicality, meaningful reproducibility, and reality check provided by the experiments [77]. Thus, future studies should include computational simulations to evaluate the potential use of GNP composites as a marine coatings.

4. Conclusions

Biofilms developed on the GNP composite had reduced wet weight, thickness, biovolume, and surface coverage in the maturation stage when compared to the control surfaces (glass and epoxy resin). Moreover, the GNP composite delayed cyanobacterial biofilm development and promoted the development of a less porous biofilm. As the graphene coating should serve as a long-term antifouling material for marine applications, the analysis of cyanobacterial biofilm behavior over time performed in this study is particularly relevant. The analysis of these GNP-based surfaces in vitro to assess their performance against mixed-species biofilms, and in situ to assess their effect on biofilm formation by additional microfoulers or to evaluate the potentially damaging effect of harsh marine environments on these nanostructured surfaces, will be performed in future studies. Therefore, upcoming tests should focus on tribological parameters such as the friction coefficient,

wear, temperature, and durability related to the application, and surface characterization for long-term assays.

Supplementary Materials: The following supporting information can be downloaded at: https://www.mdpi.com/article/10.3390/coatings12111775/s1, Figure S1: Representative 2D cross-sectional OCT images obtained for *Lusitaniella coriacea* LEGE 07157 biofilms on glass (a), epoxy resin (b), and GNP composite (c) after 28 days. The empty spaces on the biofilm structure are indicated in blue (scale bar = 100 μm).; Figure S2: Roughness coefficient[1] values of *Lusitaniella coriacea* LEGE 07157 biofilms on different surfaces: glass (black), epoxy resin (grey), and GNP composite (white). Mean values and SD from two biological assays with two technical replicates each are represented. For each surface, different lowercase letters indicate significant differences between the sampling day (day 28 vs. day 49; $p < 0.05$; unpaired t-test). The p value obtained for glass and epoxy resin was < 0.0001, and for GNP composite was 0.0104.

Author Contributions: Conceptualization, M.J.R. and F.J.M.; methodology, M.J.R., L.C.G. and F.S.-C.; formal analysis, M.J.R. and L.C.G.; investigation, M.J.R. and L.C.G.; resources, M.F.R.P., V.V., K.A.W. and F.J.M.; funding acquisition, M.F.R.P., V.V. and F.J.M.; data curation, M.J.R. and L.C.G.; writing—original draft preparation, M.J.R. and L.C.G.; writing—review and editing, J.M., M.F.R.P., O.S.G.P.S., K.A.W. and F.J.M.; supervision, V.V. and F.J.M. All authors have read and agreed to the published version of the manuscript.

Funding: This research was funded by: LA/P/0045/2020 (ALiCE), UIDB/00511/2020 and UIDP/00511/2020 (LEPABE) and project PTDC/CTM-COM/4844/2020, funded by national funds through FCT/MCTES (PIDDAC); project HealthyWaters (NORTE-01-0145-FEDER-000069), supported by Norte Portugal Regional Operational Programme (NORTE 2020), under the PORTUGAL 2020 Partnership Agreement, through the European Regional Development Fund (ERDF); Strategic Funding UIDB/04423/2020 and UIDP/04423/2020 through national funds provided by the Foundation for Science and Technology (FCT); ATLANTIDA (NORTE-01-0145-FEDER-000040), financed by the FEDER through the NORTE 2020 Program and the European Regional Development Fund (ERDF) in the framework of the program PT2020; project SurfSAFE supported by the European Union's Horizon 2020 Research and Innovation Programme under grant agreement no. 952471. M.J.R, L.C.G., and O.S.G.P.S. thank FCT for the financial support of a Ph.D. grant (SFRH/BD/140080/2018), and work contracts through the Scientific Employment Stimulus—Individual Call—[CEECIND/01700/2017] and the Scientific Employment Stimulus—Institutional Call—CEECINST/00049/2018, respectively. Support from the EURO-MIC COST Action (CA20130) is also acknowledged.

Institutional Review Board Statement: Not applicable.

Informed Consent Statement: Not applicable.

Data Availability Statement: The data presented in this study are available from the corresponding author upon request.

Conflicts of Interest: The authors declare no conflict of interest.

References

1. Schultz, M.P.; Bendick, J.A.; Holm, E.R.; Hertel, W.M. Economic impact of biofouling on a naval surface ship. *Biofouling* **2011**, *27*, 87–98. [CrossRef]
2. Delauney, L.; Compère, C.; Lehaitre, M. Biofouling protection for marine environmental sensors. *Ocean Sci.* **2010**, *6*, 503–511. [CrossRef]
3. Giakoumi, S.; Katsanevakis, S.; Albano, P.G.; Azzurro, E.; Cardoso, A.C.; Cebrian, E.; Deidun, A.; Edelist, D.; Francour, P.; Jimenez, C.; et al. Management priorities for marine invasive species. *Sci. Total Environ.* **2019**, *688*, 976–982. [CrossRef] [PubMed]
4. Bannister, J.; Sievers, M.; Bush, F.; Bloecher, N. Biofouling in marine aquaculture: A review of recent research and developments. *Biofouling* **2019**, *35*, 631–648. [CrossRef] [PubMed]
5. Kumar, S.; Bhattacharya, W.; Singh, M.; Halder, D.; Mitra, A. Plant latex capped colloidal silver nanoparticles: A potent anti-biofilm and fungicidal formulation. *J. Mol. Liq.* **2017**, *230*, 705–713. [CrossRef]
6. Zhang, D.; Liu, Z.; Wu, G.; Yang, Z.; Cui, Y.; Li, H.; Zhang, Y. Fluorinated carbon nanotube superamphiphobic coating for high-efficiency and long-lasting underwater antibiofouling surfaces. *ACS Appl. Bio Mater.* **2021**, *4*, 6351–6360. [CrossRef] [PubMed]
7. Jin, H.; Zhang, T.; Bing, W.; Dong, S.; Tian, L. Antifouling performance and mechanism of elastic graphene-silicone rubber composite membranes. *J. Mater. Chem. B* **2018**, *7*, 488–497. [CrossRef]

8. Kumar, S.; Boro, J.C.; Ray, D.; Mukherjee, A.; Dutta, J. Bionanocomposite films of agar incorporated with ZnO nanoparticles as an active packaging material for shelf life extension of green grape. *Heliyon* **2019**, *5*, e01867. [CrossRef]
9. Kim, J.; Baek, Y.; Hong, S.P.; Yoon, H.; Kim, S.; Kim, C.; Kim, J.; Yoon, J. Evaluation of thin-film nanocomposite RO membranes using TiO_2 nanotubes and TiO_2 nanoparticles: A comparative study. *Desalin. Water Treat.* **2016**, *57*, 24674–24681. [CrossRef]
10. Callow, J.A.; Callow, M.E. Trends in the development of environmentally friendly fouling-resistant marine coatings. *Nat. Commun.* **2011**, *2*, 244. [CrossRef]
11. Al-Jumaili, A.; Alancherry, S.; Bazaka, K.; Jacob, M.V. Review on the antimicrobial properties of carbon nanostructures. *Materials* **2017**, *10*, 1066. [CrossRef]
12. Xu, H.; Ma, L.; Jin, Z. Nitrogen-doped graphene: Synthesis, characterizations and energy applications. *J. Energy Chem.* **2018**, *27*, 146–160. [CrossRef]
13. Parra, C.; Montero-Silva, F.; Henríquez, R.; Flores, M.; Garín, C.; Ramírez, C.; Moreno, M.; Correa, J.; Seeger, M.; Häberle, P. Suppressing bacterial interaction with copper surfaces through graphene and hexagonal-boron nitride coatings. *ACS Appl. Mater. Interfaces* **2015**, *7*, 6430–6437. [CrossRef]
14. Naddaf, A.; Heris, S.Z.; Pouladi, B. An experimental study on heat transfer performance and pressure drop of nanofluids using graphene and multi-walled carbon nanotubes based on diesel oil. *Powder Technol.* **2019**, *352*, 369–380. [CrossRef]
15. Smaradhana, D.F.; Prabowo, A.R.; Ganda, A.N.F. Exploring the potential of graphene materials in marine and shipping industries—A technical review for prospective application on ship operation and material-structure aspects. *J. Ocean Eng. Sci.* **2021**, *6*, 299–316. [CrossRef]
16. Pan, L.; Liu, S.; Oderinde, O.; Li, K.; Yao, F.; Fu, G. Facile fabrication of graphene-based aerogel with rare earth metal oxide for water purification. *Appl. Surf. Sci.* **2018**, *427*, 779–786. [CrossRef]
17. Hu, M.; Cui, Z.; Li, J.; Zhang, L.; Mo, Y.; Dlamini, D.S.; Wang, H.; He, B.; Li, J.; Matsuyama, H. Ultra-low graphene oxide loading for water permeability, antifouling and antibacterial improvement of polyethersulfone/sulfonated polysulfone ultrafiltration membranes. *J. Colloid Interface Sci.* **2019**, *552*, 319–331. [CrossRef] [PubMed]
18. Balaure, P.C. Special Issue: Advances in engineered nanostructured antibacterial surfaces and coatings. *Coatings* **2022**, *12*, 1041. [CrossRef]
19. Selim, M.S.; El-Safty, S.A.; Fatthallah, N.A.; Shenashen, M.A. Silicone/graphene oxide sheet-alumina nanorod ternary composite for superhydrophobic antifouling coating. *Prog. Org. Coatings* **2018**, *121*, 160–172. [CrossRef]
20. Selim, M.S.; Fatthallah, N.A.; Higazy, S.A.; Hao, Z.; Mo, P.J. A comparative study between two novel silicone/graphene-based nanostructured surfaces for maritime antifouling. *J. Colloid Interface Sci.* **2022**, *606*, 367–383. [CrossRef]
21. Gu, J.; Li, L.; Huang, D.; Jiang, L.; Liu, L.; Li, F.; Pang, A.; Guo, X.; Tao, B. In situ synthesis of graphene@cuprous oxide nanocomposite incorporated marine antifouling coating with elevated antifouling performance. *Open J. Org. Polym. Mater.* **2019**, *9*, 47–62. [CrossRef]
22. Li, Y.; Huang, Y.; Wang, F.; Liang, W.; Yang, H.; Wu, D. Fabrication of acrylic acid modified graphene oxide (AGO)/acrylate composites and their synergistic mechanisms of anticorrosion and antifouling properties. *Prog. Org. Coatings* **2022**, *168*, 106910. [CrossRef]
23. Zhang, Z.; Chen, R.; Song, D.; Yu, J.; Sun, G.; Liu, Q.; Han, S.; Liu, J.; Zhang, H.; Wang, J. Guanidine-functionalized graphene to improve the antifouling performance of boron acrylate polymer. *Prog. Org. Coatings* **2021**, *159*, 106396. [CrossRef]
24. Jin, H.; Bing, W.; Tian, L.; Wang, P.; Zhao, J. Combined effects of color and elastic modulus on antifouling performance: A study of graphene oxide/silicone rubber composite membranes. *Materials* **2019**, *12*, 2608. [CrossRef] [PubMed]
25. Liu, Z.; Tian, S.; Li, Q.; Wang, J.; Pu, J.; Wang, G.; Zhao, W.; Feng, F.; Qin, J.; Ren, L. Integrated dual-functional ormosil coatings with AgNPs@rGO nanocomposite for corrosion resistance and antifouling applications. *ACS Sustain. Chem. Eng.* **2020**, *8*, 6786–6797. [CrossRef]
26. Zhang, X.; Mikkelsen, Ø. Graphene oxide/silver nanocomposites as antifouling coating on sensor housing materials. *J. Clust. Sci.* **2021**, *33*, 627–635. [CrossRef]
27. Sousa-Cardoso, F.; Teixeira-Santos, R.; Mergulhão, F.J.M. Antifouling performance of carbon-based coatings for marine applications: A systematic review. *Antibiotics* **2022**, *11*, 1102. [CrossRef]
28. Yee, M.S.-L.; Khiew, P.-S.; Chiu, W.S.; Tan, Y.F.; Kok, Y.-Y.; Leong, C.-O. Green synthesis of graphene-silver nanocomposites and its application as a potent marine antifouling agent. *Colloids Surf. B Biointerfaces* **2016**, *148*, 392–401. [CrossRef]
29. Jiang, T.; Qi, L.; Qin, W. Improving the environmental compatibility of marine sensors by surface functionalization with graphene oxide. *Anal. Chem.* **2019**, *91*, 13268–13274. [CrossRef] [PubMed]
30. Parra, C.; Dorta, F.; Jimenez, E.; Henríquez, R.; Ramírez, C.; Rojas, R.; Villalobos, P. A nanomolecular approach to decrease adhesion of biofouling-producing bacteria to graphene-coated material. *J. Nanobiotechnol.* **2015**, *13*, 82. [CrossRef]
31. Krishnamoorthy, K.; Jeyasubramanian, K.; Premanathan, M.; Subbiah, G.; Shin, H.S.; Kim, S.-J. Graphene oxide nanopaint. *Carbon N. Y.* **2014**, *72*, 328–337. [CrossRef]
32. Balakrishnan, A.; Jena, G.; George, R.P.; Philip, J. Polydimethylsiloxane-graphene oxide nanocomposite coatings with improved anti-corrosion and anti-biofouling properties. *Environ. Sci. Pollut. Res.* **2020**, *28*, 7404–7422. [CrossRef]
33. Manderfeld, E.; Kleinberg, M.N.; Thamaraiselvan, C.; Koschitzki, F.; Gnutt, P.; Plumere, N.; Arnusch, C.J.; Rosenhahn, A. Electrochemically activated laser-induced graphene coatings against marine biofouling. *Appl. Surf. Sci.* **2021**, *569*, 150853. [CrossRef]

34. Fazli-Shokouhi, S.; Nasirpouri, F.; Khatamian, M. Epoxy-matrix polyaniline/*p*-phenylenediamine-functionalised graphene oxide coatings with dual anti-corrosion and anti-fouling performance. *RSC Adv.* **2021**, *11*, 11627–11641. [CrossRef] [PubMed]
35. Chambers, L.D.; Stokes, K.R.; Walsh, F.C.; Wood, R.J.K. Modern approaches to marine antifouling coatings. *Surf. Coat. Technol.* **2006**, *201*, 3642–3652. [CrossRef]
36. Palmer, J.; Flint, S.; Brooks, J. Bacterial cell attachment, the beginning of a biofilm. *J. Ind. Microbiol. Biotechnol.* **2007**, *34*, 577–588. [CrossRef]
37. Mostafaei, A.; Nasirpouri, F. Preparation and characterization of a novel conducting nanocomposite blended with epoxy coating for antifouling and antibacterial applications. *J. Coatings Technol. Res.* **2013**, *10*, 679–694. [CrossRef]
38. Hoge, J.; Leach, C. Epoxy resin infused boat hulls. *Reinf. Plast.* **2016**, *60*, 221–223. [CrossRef]
39. Faria, S.I.; Teixeira-Santos, R.; Gomes, L.C.; Silva, E.R.; Morais, J.; Vasconcelos, V.; Mergulhão, F.J.M. Experimental assessment of the performance of two marine coatings to curb biofilm formation of microfoulers. *Coatings* **2020**, *10*, 893. [CrossRef]
40. Oliveira, I.M.; Gomes, M.; Gomes, L.C.; Pereira, M.F.R.; Soares, O.S.G.P.; Mergulhão, F.J. Performance of graphene/polydimethylsiloxane surfaces against *S. aureus* and *P. aeruginosa* single- and dual-species biofilms. *Nanomaterials* **2022**, *12*, 355. [CrossRef]
41. Faria, S.I.; Teixeira-Santos, R.; Romeu, M.J.; Morais, J.; Vasconcelos, V.; Mergulhão, F.J. The relative importance of shear forces and surface hydrophobicity on biofilm formation by coccoid cyanobacteria. *Polymers* **2020**, *12*, 653. [CrossRef] [PubMed]
42. Romeu, M.J.; Lima, M.; Gomes, L.C.; de Jong, E.D.; Vasconcelos, V.; Pereira, M.F.R.; Soares, O.S.G.P.; Sjollema, J.; Mergulhão, F.J. The use of 3D optical coherence tomography to analyze the architecture of cyanobacterial biofilms formed on a carbon nanotube composite. *Polymers* **2022**, *14*, 4410. [CrossRef] [PubMed]
43. Whitehead, K.; Kelly, P.; Li, H.; Verran, J. Surface topography and physicochemistry of silver containing titanium nitride nanocomposite coatings. *J. Vac. Sci. Technol. B Nanotechnol. Microelectron. Mater. Process. Meas. Phenom.* **2010**, *28*, 180. [CrossRef]
44. Skovager, A.; Whitehead, K.; Siegumfeldt, H.; Ingmer, H.; Verran, J.; Arneborg, N. Influence of flow direction and flow rate on the initial adhesion of seven *Listeria monocytogenes* strains to fine polished stainless steel. *Int. J. Food Microbiol.* **2012**, *157*, 174–181. [CrossRef] [PubMed]
45. Ramos, V.; Morais, J.; Castelo-Branco, R.; Pinheiro, Â.; Martins, J.; Regueiras, A.; Pereira, A.L.; Lopes, V.R.; Frazão, B.; Gomes, D.; et al. Cyanobacterial diversity held in microbial biological resource centers as a biotechnological asset: The case study of the newly established LEGE culture collection. *J. Appl. Phycol.* **2018**, *30*, 1437–1451. [CrossRef]
46. Kotai, J. Instructions for the Preparation of Modified Nutrient Solution Z8 for Algae. *Nor. Inst. Water Res.* **1972**, *11*, 5.
47. Romeu, M.J.; Alves, P.; Morais, J.; Miranda, J.M.; de Jong, E.D.; Sjollema, J.; Ramos, V.; Vasconcelos, V.; Mergulhão, F.J.M. Biofilm formation behaviour of marine filamentous cyanobacterial strains in controlled hydrodynamic conditions. *Environ. Microbiol.* **2019**, *21*, 4411–4424. [CrossRef]
48. Boyer, J.N.; Kelble, C.R.; Ortner, P.B.; Rudnick, D.T. Phytoplankton bloom status: Chlorophyll a biomass as an indicator of water quality condition in the southern estuaries of Florida, USA. *Ecol. Indic.* **2009**, *9*, S56–S67. [CrossRef]
49. Porra, R.J.; Thompson, W.A.; Kriedemann, P.E. Determination of accurate extinction coefficients and simultaneous equations for assaying chlorophylls a and b extracted with four different solvents: Verification of the concentration of chlorophyll standards by atomic absorption spectroscopy. *Biochim. Biophys. Acta BBA Bioenerg.* **1989**, *975*, 384–394. [CrossRef]
50. Bakker, D.P.; Van der Plaats, A.; Verkerke, G.J.; Busscher, H.J.; Mei, H.C. Van der comparison of velocity profiles for different flow chamber designs used in studies of microbial adhesion to surfaces. *Appl. Environ. Microbiol.* **2003**, *69*, 6280–6287. [CrossRef]
51. Silva, E.R.; Tulcidas, A.V.; Ferreira, O.; Bayón, R.; Igartua, A.; Mendoza, G.; Mergulhão, F.J.; Faria, S.I.; Gomes, L.C.; Carvalho, S.; et al. Assessment of the environmental compatibility and antifouling performance of an innovative biocidal and foul-release multifunctional marine coating. *Environ. Res.* **2021**, *198*, 111219. [CrossRef] [PubMed]
52. Romeu, M.J.; Domínguez-Pérez, D.; Almeida, D.; Morais, J.; Araújo, M.J.; Osório, H.; Campos, A.; Vasconcelos, V.; Mergulhão, F.J. Hydrodynamic conditions affect the proteomic profile of marine biofilms formed by filamentous cyanobacterium. *NPJ Biofilms Microbiomes* **2022**, *8*, 80. [CrossRef] [PubMed]
53. Faria, S.; Gomes, L.C.; Teixeira-Santos, R.; Morais, J.; Vasconcelos, V.; Mergulhão, F. Developing new marine antifouling surfaces: Learning from single-strain laboratory tests. *Coatings* **2021**, *11*, 90. [CrossRef]
54. Romeu, M.J.L.; Domínguez-Pérez, D.; Almeida, D.; Morais, J.; Campos, A.; Vasconcelos, V.; Mergulhão, F.J.M. Characterization of planktonic and biofilm cells from two filamentous cyanobacteria using a shotgun proteomic approach. *Biofouling* **2020**, *36*, 631–645. [CrossRef]
55. Faria, S.; Teixeira-Santos, R.; Romeu, M.J.; Morais, J.; Jong, E.; Sjollema, J.; Vasconcelos, V.; Mergulhão, F.J. Unveiling the antifouling performance of different marine surfaces and their effect on the development and structure of cyanobacterial biofilms. *Microorganisms* **2021**, *9*, 1102. [CrossRef] [PubMed]
56. Romeu, M.J.; Domínguez-Pérez, D.; Almeida, D.; Morais, J.; Araújo, M.J.; Osório, H.; Campos, A.; Vasconcelos, V.; Mergulhão, F. Quantitative proteomic analysis of marine biofilms formed by filamentous cyanobacterium. *Environ. Res.* **2021**, *201*, 111566. [CrossRef] [PubMed]
57. Heydorn, A.; Nielsen, A.T.; Hentzer, M.; Sternberg, C.; Givskov, M.; Ersbøll, B.K.; Molin, S. Quantification of biofilm structures by the novel computer program COMSTAT. *Microbiology* **2000**, *146*, 2395–2407. [CrossRef]
58. Alves, P.; Gomes, L.C.; Rodríguez-Emmenegger, C.; Mergulhão, F.J. Efficacy of a poly (MeOEGMA) brush on the prevention of *Escherichia coli* biofilm formation and susceptibility. *Antibiotics* **2020**, *9*, 216. [CrossRef]

59. Zheng, S.; Bawazir, M.; Dhall, A.; Kim, H.-E.; He, L.; Heo, J.; Hwang, G. Implication of surface properties, bacterial motility, and hydrodynamic conditions on bacterial surface sensing and their initial adhesion. *Front. Bioeng. Biotechnol.* **2021**, *9*, 643722. [CrossRef]
60. Yuan, Y.; Lee, T.R. Contact angle and wetting properties. In *Surface Science Techniques*; Springer Series in surface sciences 51; Bracco, G., Holst, B., Eds.; Springer: Berlin/Heidelberg, Germany, 2013; Volume 51, pp. 3–34. ISBN 978-3-642-34242-4.
61. Doshi, B.; Sillanpää, M.; Kalliola, S. A review of bio-based materials for oil spill treatment. *Water Res.* **2018**, *135*, 262–277. [CrossRef]
62. Rafiee, J.; Mi, X.; Gullapalli, H.; Thomas, A.V.; Yavari, F.; Shi, Y.; Ajayan, P.M.; Koratkar, N.A. Wetting transparency of graphene. *Nat. Mater.* **2012**, *11*, 217–222. [CrossRef]
63. Chatterjee, S.; Nüesch, F.A.; Chu, B.T.T. Comparing carbon nanotubes and graphene nanoplatelets as reinforcements in polyamide 12 composites. *Nanotechnology* **2011**, *22*, 275714. [CrossRef]
64. Santos, C.M.; Mangadlao, J.; Ahmed, F.; Leon, A.; Advincula, R.C.; Rodrigues, D. Graphene nanocomposite for biomedical applications: Fabrication, antimicrobial and cytotoxic investigations. *Nanotechnology* **2012**, *23*, 395101. [CrossRef]
65. Zou, X.; Zhang, L.; Wang, Z.; Luo, Y. Mechanisms of the antimicrobial activities of graphene materials. *J. Am. Chem. Soc.* **2016**, *138*, 2064–2077. [CrossRef]
66. Mohammed, H.; Kumar, A.; Bekyarova, E.; Al-Hadeethi, Y.; Zhang, X.; Chen, M.; Ansari, M.S.; Cochis, A.; Rimondini, L. Antimicrobial mechanisms and effectiveness of graphene and graphene-functionalized biomaterials. A scope review. *Front. Bioeng. Biotechnol.* **2020**, *8*, 465. [CrossRef] [PubMed]
67. Staneva, A.D.; Dimitrov, D.K.; Gospodinova, D.N.; Vladkova, T.G. Antibiofouling activity of graphene materials and graphene-based antimicrobial coatings. *Microorganisms* **2021**, *9*, 1839. [CrossRef] [PubMed]
68. Sjollema, J.; Rustema-Abbing, M.; van der Mei, H.C.; Busscher, H.J. Generalized relationship between numbers of bacteria and their viability in biofilms. *Appl. Environ. Microbiol.* **2011**, *77*, 5027–5029. [CrossRef]
69. Song, C.; Yang, C.-M.; Sun, X.-F.; Xia, P.-F.; Qin, J.; Guo, B.-B.; Wang, S.-G. Influences of graphene oxide on biofilm formation of gram-negative and gram-positive bacteria. *Environ. Sci. Pollut. Res.* **2017**, *25*, 2853–2860. [CrossRef] [PubMed]
70. Ahmed, B.; Ameen, F.; Rizvi, A.; Ali, K.; Sonbol, H.; Zaidi, A.; Khan, M.S.; Musarrat, J. Destruction of cell topography, morphology, membrane, inhibition of respiration, biofilm formation, and bioactive molecule production by nanoparticles of Ag, ZnO, CuO, TiO_2, and Al_2O_3 toward beneficial soil bacteria. *ACS Omega* **2020**, *5*, 7861–7876. [CrossRef]
71. Fatima, N.; Qazi, U.Y.; Mansha, A.; Bhatti, I.A.; Javaid, R.; Abbas, Q.; Nadeem, N.; Rehan, Z.A.; Noreen, S.; Zahid, M. Recent developments for antimicrobial applications of graphene-based polymeric composites: A review. *J. Ind. Eng. Chem.* **2021**, *100*, 40–58. [CrossRef]
72. Radhi, A.; Mohamad, D.; Rahman, F.S.A.; Abdullah, A.M.; Hasan, H. Mechanism and factors influence of graphene-based nanomaterials antimicrobial activities and application in dentistry. *J. Mater. Res. Technol.* **2021**, *11*, 1290–1307. [CrossRef]
73. Azizi-Lalabadi, M.; Hashemi, H.; Feng, J.; Jafari, S.M. Carbon nanomaterials against pathogens; the antimicrobial activity of carbon nanotubes, graphene/graphene oxide, fullerenes, and their nanocomposites. *Adv. Colloid Interface Sci.* **2020**, *284*, 102250. [CrossRef]
74. Mountcastle, S.E.; Vyas, N.; Villapun, V.M.; Cox, S.C.; Jabbari, S.; Sammons, R.L.; Shelton, R.M.; Walmsley, A.D.; Kuehne, S.A. Biofilm viability checker: An open-source tool for automated biofilm viability analysis from confocal microscopy images. *NPJ Biofilms Microbiomes* **2021**, *7*, 44. [CrossRef] [PubMed]
75. Van den Driessche, F.; Rigole, P.; Brackman, G.; Coenye, T. Optimization of resazurin-based viability staining for quantification of microbial biofilms. *J. Microbiol. Methods* **2014**, *98*, 31–34. [CrossRef]
76. Ammarullah, M.I.; Santoso, G.; Sugiharto, S.; Supriyono, T.; Wibowo, D.B.; Kurdi, O.; Tauviqirrahman, M.; Jamari, J. Minimizing risk of failure from ceramic-on-ceramic total hip prosthesis by selecting ceramic materials based on tresca stress. *Sustainability* **2022**, *14*, 13413. [CrossRef]
77. Dingreville, R.; Karnesky, R.A.; Puel, G.; Schmitt, J.-H. Synergies between computational modeling and experimental characterization of materials across length scales. *J. Mater. Sci.* **2015**, *51*, 1176–1177. [CrossRef]